Estimation of sinking velocities using free-falling dynamically scaled models: foraminifera as a test case

Matthew Walker[1*], Jörg U Hammel[2], Fabian Wilde[2], Tatjana Hoehfurtner[1], Stuart Humphries[1] and Rudi Schuech[1,3]

[1]School of Life Sciences, Joseph Banks Laboratories, University of Lincoln, Green Lane, Lincoln, UK

[2] Institute of Materials Research, Helmholtz-Zentrum Geesthacht, Outstation at DESY, Building 66, Notkestr. 85, D-22607 Hamburg, Germany

[3]Current Address: Center for Computational Science, Stanley Thomas Hall 405, Tulane University, 6823 St. Charles Ave, New Orleans, LA 70118, USA

*matthewwalkerbio@gmail.com

Key words: hydrodynamics, settling, dynamic scaling, model, foraminifera

Summary Statement

We developed a novel method to determine the sinking velocity of biologically important micro-scale particles using 3D printed scale models.

Abstract

The velocity of settling particles is an important determinant of distribution in extinct and extant species with passive dispersal mechanisms, such as plants, corals, and phytoplankton. Here we adapt dynamic scaling, borrowed from engineering, to determine settling velocities. Dynamic scaling leverages physical models with relevant dimensionless numbers matched to achieve similar dynamics to the original object. Previous studies have used flumes, wind tunnels, or towed models to examine fluid flows around objects with known velocities. Our novel application uses free-falling models to determine the unknown sinking velocities of planktonic foraminifera – organisms important to our understanding of the Earth's current and historic climate. Using enlarged 3D printed models of microscopic foraminifera tests, sunk in viscous mineral oil to match their Reynolds numbers and drag coefficients, we predict sinking velocities of real tests in seawater. This method can be applied to study other settling particles such as plankton, spores, or seeds.

Introduction

The transport of organisms and biologically derived particles through fluid environments strongly influences their spatiotemporal distributions and ecology. In up to a third of terrestrial plants (Willson et al., 1990), reproduction is achieved through passive movement of propagules (e.g., seeds) on the wind. In aquatic environments, propagules of many sessile groups from corals (Jones et al., 2015) to bivalves (Booth, 1983) are dispersed by ambient currents, eventually settling out of the water column to their final locations. Furthermore, most dead aquatic organisms (from diatoms to whales) sink, transporting nutrients to deeper water and contributing to long term storage of carbon (De La Rocha & Passow, 2007). In the case of microfossils, sinking dynamics of the original organisms even influences our reconstructions of the Earth's paleoclimate (Van Sebille et al., 2015). Crucially, the horizontal distances over which all these biological entities are transported, and therefore their distributions, are affected by their settling velocities (Ali et al., 2011).

Measuring the individual settling velocities of small particles directly is challenging, especially when they are too small to be imaged easily without magnification (e.g. Walsby and Holland, 2006). Here we apply dynamic scaling, an approach commonly used in engineering, to circumvent this difficulty and accurately quantify the kinematics of sub-millimeter scale free-falling particles using enlarged physical models. We use scaled-up physical models in a high-viscosity fluid, enabling easy measurements of settling speed, orientation, and other parameters using inexpensive standard high-definition web cameras. While dynamically scaled models have previously been employed to study a number of problems in biological fluid mechanics (e.g. Vogel, Ellington and Kilgore, 1973; Vogel, 1987; Vogel, 1994; Koehl, 2003), the study of freely-falling particles of complex shape – for which settling speed is the key unknown parameter – presents a unique challenge to experimental design that we overcome in this work.

Engineering problems such as aircraft and submarine design often are approached using scaled-down models in wind tunnels or flumes to examine fluid flows around the model and the resulting fluid dynamic forces it is subjected to. To ensure that the behaviour of the model system is an accurate representation of real life, similarity of relevant physical phenomena must be maintained between the two. If certain dimensionless numbers (i.e., ratios of physical quantities such that all dimensional units cancel) that describe the system are equal between the life-size original and the scaled-down model, “similitude” is achieved and all parameters of interest (e.g., velocities and forces) will be proportional between prototype and model (Zohuri, 2015). Intuitively, the model and real object must be geometrically similar (i.e., have the same shape), so that the dimensionless ratio of any length between model and original, $Length_{model}/Length_{real}$, is constant – this is the scale factor (S) of the model. Less obvious is the additional requirement of dynamic similarity, signifying that the ratios of all relevant forces are constant. For completely immersed objects sinking steadily at terminal velocity (achieved quickly for most small particles, see Time to Terminal Velocity), dynamic similarity is achieved by matching the Reynolds number (Re).

Re is a measure of the ratio of inertial to viscous forces in the flow (Batchelor, 2000; within a biological context Vogel, 1994), and is typically defined as:

$$Re = \frac{L\ U\ \rho_{fluid}}{\mu} \tag{1}$$

where ρ_{fluid} is density of the fluid (kg m^{-3}); L is a characteristic length (m) of the object; U is the object’s velocity (m s^{-1}); and μ is the dynamic viscosity (N s m^{-2}, or Pa s) of the fluid. In cases where $L\ U\ \rho_{fluid}$ is large compared to μ, e.g. whales, birds, and fish ($Re \approx 3\times10^{9}$ - 3×10^{6}, Vogel, 1994), inertial forces dominate. In cases where $L\ U\ \rho_{fluid}$ is relatively small compared to μ, e.g. sperm, bacteria (Re $\approx 3\times10^{-2}$ - 1×10^{-5}), viscous forces dominate. Finally, when $L\ U\ \rho_{fluid}$ is of comparable magnitude to μ, Re is intermediate and one cannot discount either inertial or viscous forces. If the scaled model and original system exhibit identical Re, the relative importance of inertial versus viscous forces is matched between the two and any qualitative features of the flows (e.g. streamlines) will also be identical.

Dynamically scaled physical models exhibiting the same Re as the original systems have been used in a number of biological studies. Vogel and La Barbera (1978) outline the principles of dynamic scaling: to obtain the same Re when enlarging small organisms, the fluid flow must be slower and/or the fluid more viscous, and when making smaller models of large organisms, the fluid flow must be faster and/or the fluid less viscous. For instance, Vogel (1987) used air in place of water flowing at lower speeds when investigating the refilling of the squids mantle during swimming by scaling a model up 1.5 times relative to the animal’s actual size. More recently, Stadler et al (2016) investigated sand inhalation in skinks with 3D-printed enlarged models, using helium instead of air (thereby increasing viscosity) as the experimental fluid. Koehl and colleagues have studied crustacean antennule flicking (lobsters (Reidenbach et al., 2008), mantis shrimp (Stacey et al., 2002) and crabs (Waldrop et al., 2015)) as well as the movements of copepod appendages (Koehl, 1995) with enlarged models, using mineral oil in place of water. Finally, perhaps the largest change in scale was employed by Kim et al (2003), who modelled the bundling of *E. coli* flagella at a scale factor of ~61,000, submerged in silicone oil (10^5 times more viscous than water), and rotated at 0.002 rpm compared to the 600 rpm observed in real bacteria (Sowa & Berry, 2008).

In all the above studies, basic kinematics such as speeds in the original system were relatively easy to measure, and the experiments aimed to reveal the forces involved (e.g. hydrodynamic drag) or details of the fluid flow such as the pattern of streamlines. Since the representative speed U of the original system was known, designing experiments to achieve similitude was relatively straightforward because the Re was also known *a priori* – in these cases, the model size, speed, and working fluid properties were simply interrelated through Re (Eqn 1). For instance, once a working fluid and the model size were chosen, the required towing speed was obvious. However, in the case of sedimentation of small particles (e.g. spores, seeds, plankton), the sinking speed (U) is the key unknown. With an unknown sinking speed, the operating Re is also unknown, so it is not straightforward to design experiments that achieve similitude with the original system. Here we present an iterative methodology leveraging 3D printed dynamically scaled models that allows determination of the sinking speeds of small objects of arbitrarily complex shape.

We use planktonic foraminifera as an example of a small (200 – 1500 μm) biological particle for which the settling velocity is important and typically unknown. Foraminifera are a phylum of marine ameboid protists (B. K. Sen Gupta (ed.) , 2002; Schiebel & Hemleben, 2005). By secreting calcium carbonate, foraminifera produce a multi-chambered shell (test) which, in planktonic foraminifera, can grow up to 1500 μm in diameter, and which frequently exhibits complex shape (Table 1). Once the organism dies or undergoes reproduction, the empty test sinks to the ocean floor, and so oceanic sediments contain substantial numbers of foraminifera tests. Foraminifera account for 23-56% of the oceans production of carbonate (CO_3) (Schiebel, 2002), an important factor in climate change models (Passow & Carlson, 2012). Of particular interest for climate predictions is calculating the flux of tests reaching the ocean floor (Schiebel, 2002; Jonkers & Kučera, 2015). While there are more than 30 extant species and over 600 species in the fossil record, settling velocities are known for only 14 species of foraminifera (Fok-Pun & Komar, 1983; Takahashi & Be, 1984; Caromel et al., 2014, 3.41×10^{-4} - 6.8×10^{-2} m s^{-1}, $\mathrm{Re} \approx 18$ – 55).

Materials and Methods

Similitude and Settling Theory

We assume that the size (i.e., L – defined as the maximum length parallel to the settling direction, A – defined as the projected frontal area, and V – the particle volume not including any fluid-filled cavities), 3D shape (Ψ, here treated as a categorical variable due to our consideration of arbitrarily complex morphologies, see Table 1), and density ($\rho_{particle}$) of the original sinking particle are known, while the sinking speed (U) is unknown. The properties of the fluid surrounding the original particle (i.e. ρ_{fluid} , μ) are also known, and our goal is to design experiments in which we sink a scaled-up model particle in a working fluid of known ρ_{fluid} and μ in order to determine the model particle's sedimentation speed and, via similitude, U of the original particle.

While previous work (Berger et al., 1972; Fok-Pun & Komar, 1983; Takahashi & Be, 1984; Caromel et al., 2014) suggests that the Re of sinking forams should be $10^0 - 10^2$, the exact value of Re for morphology Ψ is assumed to be unknown. Hence, it is not immediately clear what size the model should be (i.e., the scale factor $S = L_{model}/L_{real}$) in order to match this Re in the experiments and ensure similitude. Solving for both Re and S simultaneously requires additional mathematical relationships beyond Eqn 1.

Throughout, we use a superscript O to refer to the *Original* values of dimensioned variables at life size (e.g., L^O, V^O, A^O, $\rho^O_{particle}$, U^O) and Re^O, C_D^O for the values of the dimensionless Reynolds number and drag coefficient (defined below) corresponding to real particles sinking in the original fluid (e.g., seawater of ρ^O_{fluid}, μ^O). While the fluid dynamics of flow around a particle of particular shape Ψ can be considered theoretically over a range of Re, only the dynamics at Re^O and C_D^O will represent the "operating point" corresponding to the life size particle settling speed U^O.

When a particle is sinking steadily at its terminal velocity, the sum of the external forces acting on the particle is zero (Eqn 2); that is, the upward drag force (F_{drag}, Eqn 3) and buoyant force ($F_{buoyancy}$, Eqn 4) must balance the weight of the particle (F_{weight}, Eqn 5):

$$\Sigma \mathrm{F} = F_{drag} + F_{buoyancy} - F_{weight} = 0 \tag{2}$$

where

$$F_{drag} = {}^{1}\!/_{2}\, C_D(\Psi, Re)\, \rho_{fluid} U^2 A \tag{3}$$

Eqn 3 introduces the drag coefficient $C_D(\Psi, Re)$, a dimensionless descriptor of how streamlined an object is. Both C_D and Re must be matched to achieve similitude. C_D depends on the shape of the object Ψ, including its orientation relative to the freestream flow – for instance, C_D of a flat plate oriented parallel to laminar flow is as low as 0.003 while C_D of a flat plate oriented perpendicular to the flow is ~ 2.0 (Munson et al., 1994). However, in addition to object geometry, C_D also depends on qualitative characteristics of the flow, such as whether it is laminar or turbulent – that is, C_D also depends on Re. C_D of a sphere decreases from about 200 at Re = 0.1 to about 0.5 at Re = 1000; C_D generally decreases with Re for most shapes (Munson et al., 1994; Morrison, 2013). While C_D does not depend on object size directly, larger objects generally experience higher drag forces and this is captured by the inclusion of particle area (A) in the expression for F_{drag} (Eqn 3). For brevity, we will omit Ψ hereafter and write the drag coefficient as $C_D(Re)$.

The buoyant force ($F_{buoyancy}$, Eqn 4) and weight (F_{weight}, Eqn 5) are both expressed using particle volume (V), gravitational acceleration (g), and density of the fluid (ρ_{fluid}) or particle ($\rho_{particle}$), respectively:

$$F_{buoyancy} = V \rho_{fluid}\, g \tag{4}$$

$$F_{weight} = V \rho_{particle}\, g \tag{5}$$

Substituting Eqns 3, 4, and 5 into 2 and eliminating U via the definition of Re (Eqn 1) yields an expression for the drag coefficient obtained through a force balance (indicated by a superscript $\mathcal{F}$):

$$C_D^{\mathcal{F}}(Re) = \frac{2\left(\rho_{particle} - \rho_{fluid}\right) V g}{\rho_{fluid}\, U^2 A} = \left(\frac{2\left(\rho_{particle} - \rho_{fluid}\right) V g}{\rho_{fluid}\, A}\right)\left(\frac{\rho_{fluid}\, L}{Re\, \mu}\right)^2 = \frac{2\left(\rho_{particle} - \rho_{fluid}\right) \rho_{fluid}\, V g\, L^2}{A\, Re^2\, \mu^2} \tag{6}$$

Note that this expression can be simplified further upon identification of the dimensionless Archimedes number $Ar = g\, L_{Ar}^3\, \rho_{fluid}\, (\rho_{particle} - \rho_{fluid})/\mu^2$ if the cubed length scale $L_{Ar}^3 = VL^2/A$, yielding $C_D^{\mathcal{F}}(Re) = Ar/Re^2$, as previously highlighted by others (e.g. Karamanev, 1996). However, we will proceed with the original form of Eqn 6 to keep key variables such as L explicit.

If C_D were known for a particular morphology, we could simply substitute values corresponding to the original test in seawater into Eqn 6 and solve for $Re = Re^O$ and thus U^O via Eqn 1, immediately solving the problem of unknown settling speed. Unfortunately, the complex shapes of foraminifera (Table 1) coupled with the implicit dependence of C_D on Re means that both variables are generally unknown, and thus far we have only one constraining relationship between C_D and Re. More information is required to determine where along this constraint curve the operating C_D^O and Re^O are located. This information can come from experiments in which the sinking speeds of scaled-up model particles of various sizes (i.e., scale factors S) in a viscous fluid are measured directly, allowing us to calculate Re via Eqn 1 and then $C_D^{\mathcal{F}}(Re)$ via Eqn 6 for the models, with appropriate values substituted for each experiment. For clarity, we can rewrite Eqn 6 for a model in terms of S and the original test parameters (L^O, A^O, V^O):

$$C_D^{\mathcal{F}}(Re) = \frac{2\left(\rho_{particle} - \rho_{fluid}\right) \rho_{fluid}\, (V)\, g\, (S\, L^O)^2}{(S^2\, A^O)\, Re^2\, \mu^2} \tag{7}$$

where we use the fact that for a model, $L = S\, L^O$ and $A = S^2 A^O$. While one would also expect $V = S^3\, V^O$ for 3D printed models, limitations of our 3D printer led to variation in V that we overcame using a more general empirical relationship between S and V based on mass measurements – see 3D Printer Limitations. Eqn 7 represents a constraining relationship between C_D and Re for the sinking particle, which we use to collect (Re, C_D) experimental data points at several S. Once sufficient data are collected, we can construct a new, empirical relationship (e.g., a cubic spline fit) between C_D and Re for a particular particle shape, which we term $C_D^E(Re)$. Finally, we can solve for the operating Re^O, C_D^O, and U^O by finding the intersection point between the $C_D^{\mathcal{F}}(Re)$ constraint curve specific to life-size particles sinking in seawater (i.e., Eqn 7 with S = 1 and $\rho_{particle}^O, \rho_{fluid}^O, \mu^O$) and our empirical $C_D^E(Re)$

spline curve valid for a particular particle shape moving steadily through any fluid. MATLAB code can be downloaded from https://github.com/matthewwalkerbio/Dynamic-scaling.

Study Species

To construct an empirical $C_D^E(Re)$ curve for a particular test morphology, we started with 3D scans of individual specimens from 30 different species (Table 1). The majority of the species were selected from the University of Tohoku museum's database, eforam Stock (http://webdb2.museum.tohoku.ac.jp/e-foram/), with a micro computed tomography (µCT) scan resolution between 2.5 and 3.6 pixels per µm, and were exported as 3D triangular mesh (STL format) files. Specimens of an additional three species were scanned using synchrotron radiation based micro-computed tomography (SRµCT). Imaging was performed at the Imaging Beamline P05 (IBL) (Greving et al., 2014; Haibel et al., 2010; Wilde et al., 2016) operated by the Helmholtz-Zentrum-Geesthacht at the storage ring PETRA III (Deutsches Elektronen Synchrotron – DESY, Hamburg, Germany). Specimens were imaged at an photon energy of 14 keV and with a sample to detector distance of 17 mm. For each tomographic scan, 900 projections at equal intervals between 0 and π were recorded. Tomographic reconstruction was done via a classical filtered back projection using the RECLBL library (Huesman et al., 1977). For processing, raw projections were binned two times resulting in an effective pixel size of the reconstructed volume of 1.44 µm. These scans were segmented and rendered using SPIERS (Sutton et al., 2012), and again exported in STL format and are avaliable from Morpho Source. Meshes of all foraminifera were manually checked in Meshlab (Callieri et al., 2012) for integrity.

For species where more than one scan was available, the scan that contained the best-preserved specimen was chosen. By only including one specimen per species, this approach neglects phenotypic plasticity which is demonstrated in planktonic foraminifera (e.g. Lohmann, 1983; Morard *et al*., 2013), but was chosen due to limitations of µCT scan availability and time constraints on the project.

3D printing and model preparation

The 3D scans allowed us to easily fabricate scaled-up (scale factor S) physical models of each specimen using a FormLabs Form1+ (Formlabs, Somerville, Massachusetts, USA) 3D printer, using FormLabs Clear Resin Version 2 (Formlabs, Somerville, Massachusetts, USA) with a layer thickness of 50 µm (see **Error! Reference source not found.**D for examples) and x-y resolution of 200 µm. Models were washed and flushed with isopropanol to remove excess resin following Formlabs' guide and allowed to air dry. Support material was removed (**Error! Reference source not found.**D.vi), and the models lightly sanded with 400 grit Wet 'n' Dry paper, followed by a final isopropanol wash to remove any remaining residue. Once dry, models were filled with mineral oil in preparation for sinking. Clear resin was chosen to allow each model to be checked for bubbles (which would increase the buoyancy of the model). Any bubbles were removed using a 30-gauge needle and syringe.

Following convention when defining the area $A_{particle}$ used in the definition of C_D (Eqn 3), we measured projected area of the sinking foraminifera. Referring to high resolution images of the sinking model (**Error! Reference source not found.**D), a digital model of the foraminifera was manually aligned to measure the projected area in a plane perpendicular to the sinking direction (**Error! Reference source not found.**D). We used the same procedure to measure the maximum length parallel to the flow (L) for the calculation of Re (**Error! Reference source not found.**D). These choices facilitated objective comparisons of C_D across morphologically diverse species, to be detailed in a future study.

3D Printer Limitations

Whilst in principle, the volume of a printed model should simply scale according to $V = S^3V^O$, due to inherent limitations of the 3D printer as well as difficulty in removing excess resin from small models, we found that this expectation was usually not satisfied, and weighing the models showed that $M/\rho_{particle} > S^3\ V^O$ where M is particle mass (**Error! Reference source not found.**C). Therefore, we estimated V of each model by weighing on an Entris 224-1S mass balance (±0.001 g) and assuming $\rho_{particle}$ was 1121.43 ± 13.73 kg m^{-3}, based on the average mass of five 1 cm^3 cubes of printed resin. Furthermore, whenever a predicted value for V at a given scale factor S was needed, i.e. in Eqn 7 (see Remaining iterations), we based this on cubic spline interpolation of our $V(S)$ data for existing models when sufficient data were available, with extrapolation based on cubic scaling of $V(S)$ if required (see **Error! Reference source not found.**C):

$$V^{predict}(S) = \begin{cases} H(S), N \geq 3 \\ S^3V^O, N < 3 \text{ or } S = 1 \end{cases} \quad (8)$$

where N is the number of existing volume measurements and H represents the cubic spline fit of V vs S. Note that because we always directly measured V by weighing after printing each model, and it is not necessary to achieve the exact Re and C_D of the operating point ($Re^O$and C_D^O) in the experiments (see Remaining iterations), the empirical spline-based volume prediction was not strictly required for our method to succeed. It merely aids in improving the rate of convergence of our iterative approach by reducing the difference between our anticipated and actual Re, C_D for each experiment.

Settling tank

The models were released in a cylindrical acrylic tank (0.9 m in diameter and 1.2 m in height) of mineral oil ("Carnation" white mineral oil, Tennants Distribution Limited, Cheetham, Manchester, UK; ρ = 830 kg m^{-3}, μ = 0.022 Pa S) filled to a depth of 1.18 m (approximately 750 L). The tank was fitted with a custom net and net retrieval system (**Error! Reference source not found.**A) to allow easy retrieval of the models after their descent, allowing each model to be sunk 5 times. Integrated to the net retrieval system was the release mechanism, which was held centrally over the tank, with the grasping parts submerged below the oil level. This ensured that each model was released in a controlled and repeatable fashion.

Particle imaging

To minimise reflections, the tank was surrounded by a black fabric tent-like structure. This also served as a dark background to facilitate visualisation of the model during descent. The tank was illuminated with a single 800 lumen LED spotlight placed underneath the tank and, as the Formlabs' Clear Resin is UV-fluorescent, two 20W "Blacklight" UV fluorescent tubes were placed above the tank.

The sinking models were recorded using two Logitech C920 HD webcams (Logitech, Lausanne, Switzerland), placed at 90° to each other (**Error! Reference source not found.**A) and recording at 960 pixels x 720 pixels and ~30 frames per second, allowing monitoring of the position and orientation of the particle in 3D as it fell. As these consumer-grade webcams use a variable frame-rate system, a custom MATLAB script was used to initiate camera recording, recording both frames and frame timestamps. Videos were recorded for 500 frames (~17 s). Sinking velocity was calculated over a central 0.8 m depth range, ensuring the model was at terminal velocity (see Time to Terminal Velocity) whilst also avoiding end effects which could slow the model as it reached the bottom of the tank. Based on observations of suspended dust, there was no discernable convection in the tank during any trials that might potentially affect sinking velocities. The curved walls of the tank introduced distortion, which was removed using the MATLAB toolbox "Camera Calibrator" (Mcandrew, 2004). Pixel size was 1.06 pixels per millimetre with a mean reprojection error of 0.5 pixels, therefore distance measurements (for calculating sinking velocities) were accurate to within 0.5 mm (0.06% of the traversed depth).

Velocity calculation

Models were tracked in distortion-corrected frames using a modified version of Trackbac (Guadayol et al., 2017; Guadayol, 2016). The per-frame centroid coordinates obtained were then paired with the timestamp values recorded to calculate average settling velocity components in 2D for each camera (below, U_x is horizontal speed from camera one, U_y is horizontal speed from camera two, and $U_{z,1}$ and $U_{z,2}$ are the vertical speeds corresponding to the two cameras). A resultant velocity magnitude was then calculated for each camera, and these two values averaged to yield a single estimate for U per experiment (Eqn 9).

$$U = \frac{1}{2}\left(\sqrt{{U_x}^2 + {U_y}^2 + {U_{z,1}}^2} + \sqrt{{U_x}^2 + {U_y}^2 + {U_{z,2}}^2}\right) \qquad (9)$$

Each model was sunk five times and a mean U was calculated from these replicates. Replicates beyond a threshold of ±5% of the median sinking velocity were discarded from this average. Each model was dropped one additional time and photographed using a Canon 1200D DSLR camera (Tokyo, Japan) mounted on a tripod close to the tank, to obtain high resolution (18 megapixels) images which were used to determine model orientation (and thus L and A) during settling (**Error! Reference source not found.**D).

Wall effects

At low Re, the effects of artificial walls in an experimental (or computational) system can be nonintuitively large and lead to substantial errors if not accounted for (Vogel, 1994). Acting as an additional source of drag, the walls several tens of particle diameters away can slow down a sinking particle and increase its apparent drag coefficient. We designed our experiments to minimise wall effects by using an 0.8 m diameter tank (**Error! Reference source not found.**A) and model diameters on the order of 1 cm. To reduce potential errors further, we applied the method of Fayon & Happel (1960; summarised in Clift et al., 1978) to convert between the apparent drag coefficient when walls are present (C_D^{wall}) and the desired drag coefficient in an unbounded domain (C_D^{∞}):

$$C_D^{\infty} \approx C_D^{walls} - \frac{24}{Re}\left(K(\lambda) - 1\right) \tag{10}$$

where

$$K(\lambda) = \frac{1 - 0.75857 \cdot \lambda^5}{1 - 2.1050\,\lambda + 2.0865\,\lambda^3 - 1.7068\,\lambda^5 + 0.72603\,\lambda^6}$$

Here, $\lambda = d/D$ where d is the diameter of the sinking particle and D is the tank diameter; we take $d = L$. While Eqn 10 is not exact, it substantially reduces the error otherwise incurred if one were to neglect wall effects entirely. Note that Eqn 10 is only valid up to about $Re = 50$, beyond which different corrections can be used (Clift et al., 1978).

We applied this correction by taking any experimentally determined C_D to equal C_D^{walls}, and using C_D^{∞} estimated according to Eqn 10 for subsequent calculations as detailed below. In our experiments, λ ranged from 0.0027 – 0.0173, yielding K between 1.0057 – 1.0377. Wall effects were therefore quite small, with C_D^{∞}/C_D^{walls} ranging from 0.993 – 0.994.

Iterative approach

First iteration

To construct an empirical cubic spline $C_D^E(Re)$ needed to solve for U^O, at least three experimental data points (corresponding to three scale factors) are needed. These first three S were chosen by using an existing empirical $C_D(Re)$ relationship for a sphere, valid for 0 < Re < 10^6 (Morrison, 2013, Fig. 8.13, page 625):

$$C_D^M(Re) = \frac{24}{Re} + \frac{2.6\left(\frac{Re}{5.0}\right)}{1 + \left(\frac{Re}{5.0}\right)^{1.52}} + \frac{0.411\left(\frac{Re}{263{,}000}\right)^{-7.94}}{1 + \left(\frac{Re}{263{,}000}\right)^{-8.00}} + \left(\frac{Re^{0.80}}{461{,}000}\right) \tag{11}$$

While morphologically complex particles such as foraminifera tests (Table 1) are not expected to behave like ideal spheres, Eqn 11 should be sufficient to provide initial guesses, after which we iterate to find the solution. We note that if the particle shapes of interest were all most similar to some other well-studied geometry (e.g., cylinders, discs, etc), using a known $C_D(Re)$ relationship for that shape could provide better initial guesses and faster convergence.

Substituting Eqn 11 into Eqn 7 (with S = 1, $V = V^O$, and $\rho^O_{particle}, \rho^O_{fluid}, \mu^O$ substituted) and moving all terms to one side, we can numerically solve (MATLAB: *fzero* function) for our first estimate of the operating Re^O. Substituting this Re back into Eqn 7 or Eqn 11 yields an estimate of the operating C^O_D. We aimed to reproduce this Re and C_D in the first experiment, excepting that we accounted for wall effects by distinguishing between C^∞_D and C^{walls}_D expected to occur in the tank. Hence, we could again substitute this Re into Eqn 7 but now with $\rho_{particle}$ corresponding to the resin model and ρ_{fluid} and μ corresponding to mineral oil, and combine this expression with Eqn 10, assuming our estimated $C_D = C^\infty_D$, $C^{\mathcal{F}}_D = C^{walls}_D$, and $\lambda = S\ L^O\ /D$. The resulting expression can be solved numerically for the first scale factor, termed S_1. Two more scale factors (S_2 and S_3), one smaller and one larger than S_1, were chosen to span expected Re values for forams from published literature (e.g. Fok-Pun & Komar, 1983; Takahashi & Be, 1984; Caromel et al., 2014) as well as Re^O for other species which had reached convergence. This procedure was intended to bound the correct S value that reproduces the operating Re^O and C^O_D of the settling particle. The three models were printed, their actual volumes V measured via weighing, and their settling velocities U experimentally measured as detailed in Appendix 3.

An empirical cubic spline curve $C^E_D(Re)$ can now be fitted (D'Errico, 2009) to these three initial (*Re*, C_D) data points, constrained to be monotonically decreasing and concave up within the limits of the data to match expectations for drag on objects at low to moderate Re. Three optimally spaced spline knots were used since this yielded excellent fits to the data as the number of data points increased. These details of the spline as well as its order (i.e., cubic vs linear) are somewhat arbitrary but we ensured that our results were sufficiently converged as to be insensitive to them (see Remaining iterations).

The operating point (Re^O, C^O_D) corresponding to the particle settling in the natural environment can be visually represented as the intersection point of the $C^{\mathcal{F}}_D(Re)$ curve defined by Eqn 7 (with $S = 1$ and $\rho^O_{particle}$, ρ^O_{fluid}, μ^O) and the empirical $C^E_D(Re)$ relationship based on our experimental data. Algebraically, the operating point is the solution to $C^{\mathcal{F}}_D(Re) = C^E_D(Re)$. We solved for Re^O numerically using a root finding algorithm (MATLAB's *fzero*) on the objective function $C^{\mathcal{F}}_D(Re) - C^E_D(Re) = 0$ and then obtained C^O_D by substituting Re^O into Eqn 7. Finally, U^O was easily determined from the definition of Re^O (Eqn 1 with U^O, L^O, and ρ^O_{fluid} substituted).

Since our first three empirical data points and fitted spline C^E_D corresponded to guessed model scale factors S, our initial operating point prediction (Re^O, C^O_D) often was not located near any of these initial points or sometimes even within the bounds of these data (in which case linear extrapolation of C^E_D was used to estimate the operating point). Therefore, to ensure the accuracy of our predicted U^O, we continued iterating with additional experiments.

Remaining iterations

The model scale factor for the N^th^ experiment was chosen by combining Eqns 7, 8, and 10 with $Re = Re^O$ and $C^{walls}_D = C^O_D$, (from the previous iteration), $C^{\mathcal{F}}_D = C^\infty_D$, and $V = V^{predict}$, and numerically solving for S. A model close to this new scale was printed and sunk, its settling velocity U recorded and Re and C_D computed, and a more accurate spline C_D^E constructed by including this new data point. The calculation of (Re^O, C_D^O) detailed in the previous section was then repeated, yielding a more accurate operating point. Overall, the aim was to tightly bound the predicted operating point with experimental data to maximize confidence in the fitted spline in this region.

The iterative process (visualized as a flowchart, **Error! Reference source not found.**B, with a specific example of convergence given in Fig. 2 C & D) was repeated until:

1) the predicted operating point was not extrapolated beyond our existing data,

2) the variation in calculated U^O between the fitting of a linear spline and cubic spline was no greater than 5%, and

3) the variation between the predicted Re^O and the closest experimentally measured Re was less than 15%.

In many cases, the difference between results based on four versus three data points was very small (Fig. 2 C, D), indicating rapid convergence and the possibility of streamlining the method further in the future. Through this method we calculated the sinking velocities of 30 species of planktonic foraminifera (Table 1).

Method Validation

Our basic methodology was first validated by 3D printing a series of spherical models (10 – 20 mm in diameter) for which the theoretical $C_D(Re)$ relationship is already well-known. In order to achieve low density (and thus low sinking velocity and low Re), these spheres were hollow and filled with oil via two small holes (of diameter 0.8% of the sphere diameter). Our empirically generated $C_D^E(Re)$ curve compares favourably with the theoretical $C_D^M(Re)$ curve (Morrison, 2010) (R^2=0.875, **Error! Reference source not found.**A), with the distance between the curves approximately constant above $Re \approx 25$. While the error grows larger at lower Re, we expected most foraminifera species to operate at $Re \approx$ 18 – 55 based on previous work (Berger et al., 1972; Fok-Pun & Komar, 1983; Takahashi & Be, 1984; Caromel et al., 2014).

To quantify errors in our approach even more directly, we then considered hypothetical hollow spherical particles with the same material density ($\rho_{particle}^O$) as foraminifera tests and a range of sizes (L^O = 750 – 1150 µm, similar to the species we studied) settling in seawater. This size range corresponds to $Re = 12 - 27$, the area where our $C_D^E(Re)$ curve is most divergent from $C_D^M(Re)$. We compared predictions of the operating U^O based on our empirical $C_D^E(Re)$ curve versus the theoretical $C_D^M(Re)$ curve for spheres as outlined above, substituting Eqn 11 for $C_D^E(Re)$ in the latter case. Maximum relative error in predicted U^O was 11.5% at *Re* = 16 (corresponding to a sphere 860 µm in diameter) while the minimum difference was 6.5% at *Re* = 27 (corresponding to a sphere of 1150 µm in diameter, **Error! Reference source not found.**A). This level of error is much smaller than the variation in U^O we predicted across the 30 foraminifera species we investigated (Table 1).

Time to Terminal Velocity

This study was concerned with predicting steady sinking speeds, but in our experiments, each model foraminifera took a finite amount of time to accelerate from rest at the point of release to its terminal sinking velocity. Since this transient portion of the sinking trajectory could introduce errors into our analysis, it is important to determine whether it affected any of our recorded data.

During the transient acceleration phase, Eqn 2 does not hold. Instead, we can revert to the more general form of Newton's second law:

$$\Sigma \mathrm{F} = F_{drag} + F_{buoyancy} - F_{weight} = -Ma = -M\frac{dU}{dt} \tag{12}$$

where $M = V\rho_{particle}$ is particle mass, and the acceleration a can be equated to the time derivative of instantaneous velocity $\frac{dU}{dt}$. A negative sign appears on the right-hand side so that we can define the downward movement as positive for convenience. We can then substitute expressions for each force as before:

$$^1/_2\, C_D(\Psi, Re)\, \rho_{fluid} U^2 A + V\, \rho_{fluid}\, g - V\, \rho_{particle}\, g = -\, M\frac{dU}{dt} \tag{13}$$

While thus far we have not assumed anything about the particle shape, to proceed further we require knowledge of $C_D(\Psi, Re)$ from vanishingly small Re (when the particle is at rest) up to the terminal velocity. Hence we will assume a spherical particle as an approximation to the model forams, so that Morrison's empirical equation (Eqn 11) can then be substituted for $C_D(\Psi, Re)$:

$$-\left\{1/2\left[\frac{24}{Re} + \frac{2.6\left(\frac{Re}{5.0}\right)}{1+\left(\frac{Re}{5.0}\right)^{1.52}} + \frac{0.411\left(\frac{Re}{263{,}000}\right)^{-7.94}}{1+\left(\frac{Re}{263{,}000}\right)^{-8.00}} + \left(\frac{Re^{0.80}}{461{,}000}\right)\right]\rho_{fluid} U^2 A + V\, \rho_{fluid}\, g - V\, \rho_{particle}\, g\right\}/M = \frac{dU}{dt} \tag{14}$$

Here we have isolated $\frac{dU}{dt}$ on the right-hand side. If the definition of $Re = \frac{L\, U\, \rho_{fluid}}{\mu}$ is inserted into 14 (not shown for brevity), one obtains an ordinary differential equation (ODE) for the unsteady velocity $U(t)$. The depth of the sphere $Z(t)$ can then be obtained by solving a second much simpler ODE:

$$U = \frac{dZ}{dt} \tag{15}$$

Both ODEs are easily solved numerically by e.g. MATLAB's *ode45* subject to the initial conditions $U(t = 0) = 0$ and $Z(t = 0) = 0$.

It is well known that as Re approaches zero in the limit of inertia-less Stokes flow, unsteadiness can only occur due to time-varying boundary conditions. Thus, a microorganism that stops actively swimming will almost instantly come to a stop, and a heavy micro-particle released from rest will almost instantly begin sinking at its terminal velocity (Purcell, 1977). As Re increases and inertia becomes increasingly important, the transient period of acceleration becomes longer. Therefore, a reasonable worst-case to examine here is the foraminifera model that sank at the highest Re.

We found *Globorotalia (Truncorotalia) truncatulinoides* to operate at Re = 42 (Table 1) but here we conservatively chose the largest scale model used to generate its $C_D^E(Re)$ spline for which S = 16 and Re = 90. Inserting this model's length L, area A, and measured volume V into 14, we obtain solutions for the time varying speed and depth of a sphere approximating this model's geometry (**Error! Reference source not found.**B). The depth corresponding to where speed equals 99.9% of the terminal velocity is approximately 4.6 cm, which is much smaller than the 19 cm between where the models were released and the edge of the cameras' fields of view for data collection. Hence, the transient acceleration of each model foraminifera should have had no effect on our data or results. Most of our models should have reached terminal velocity even sooner since they sank at lower Re, e.g. within 2.2 cm for *C. dissimilis* operating at Re = 36 (Table 1).

Results & Discussion

Here we present a novel method of determining settling speed by leveraging dynamically scaled models falling under gravity rather than being towed at a controlled speed. Applying our method to foraminifera-inspired spherical particles (**Error! Reference source not found.**A), we predict settling speeds within 11.5% of theoretical expectations (**Error! Reference source not found.**E). In **Error! Reference source not found.**C & D we present an example of convergence of our method to the operating Re^O, C_D^O, and U^O of a typical foraminifera species. There was little variation in the number of iterations required to reach convergence (mean 4, range 3-6, see Table 1), despite the morphological complexity of some species (e.g. *Globigerinoidesella fistulosa*). We suspect the higher end of this range was due to these species having forms that were particularly challenging to clean residual resin from, or the incomplete removal of air bubbles once submerged in oil.

Table 1.Predicted sinking speeds U^O for the 30 species of planktonic foraminifera included in this study, with each species shown in both spiral view and 90˚ rotation (so that the spiral view is facing to the left). [1] indicates species scanned high resolution. Scans of the remaining 27 species were obtained from The University of Tohoku museum's database. Operating Re^O and C_D^O predicted for each species are also presented, and for comparison, the theoretical C_D^M of a sphere at the same Re^O. The number of model iterations required to achieve convergence of U^O is listed (iter). Species synonyms checked at World Foramaninifera Database (Hayward et al., 2018)*.*

Image	Species	L^O (μm)	U^O (cm s^{-1})	Re^O	C_D^O	$C_D^M(Re^O)$	Iter	Image	Species	L^O (μm)	U^O (cm s^{-1})	Re^O	C_D^O	$C_D^M(Re^O)$	Iter
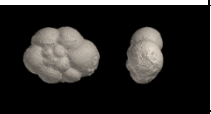	*Neogloboquadrina acostaensis* (Blow, 1959)	307	3.6	9.3	2.5	4.2	4	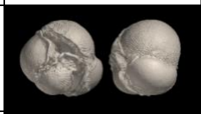	*Sphaeroidinella dehiscens* (Parker & Jones, 1865)	460	5.1	32.8	1.7	1.9	4
	*Globigerinella adamsi* (Banner & Blow, 1959)	596	3.0	9.6	2.6	4.1	4	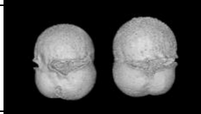	*Sphaeroidinella dehiscens*[1] (Parker & Jones, 1865)	269	2.5	8.3	5.0	4.5	4
	*Dentoglobigerina altispira* (Cushman & Jarvis, 1936)	282	6.1	37.3	1.6	1.8	5		*Catapsydrax dissimilis* (Cushman & Bermúdez, 1937)	380	6.2	36.4	1.7	1.8	4
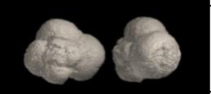	*Globoturborotalita apertura* (Cushman, 1918)	650	2.8	7.4	4.2	4.8	3	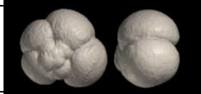	*Neogloboquadrina dutertrei* (d'Orbigny, 1839)	259	4.0	17.6	2.0	2.8	3
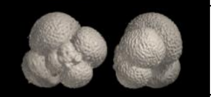	*Globigerina bulloides (d'Orbigny, 1826)*	296	3.3	13.4	2.4	3.3	5	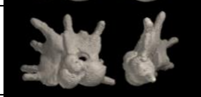	*Globigerinoidesella fistulosa* (Schubert, 1910)	392	2.6	11.2	3.0	3.7	4
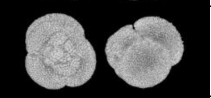	*Globigerinoides conglobatus*[1] (Brady, 1879)	445	1.8	5.8	5.9	5.7	4	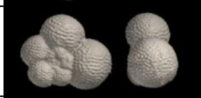	*Globorotaloides hexagonus* (Natland, 1938)	321	2.7	8.3	3.4	4.5	4
	*Globorotalia (Truncorotalia) crassaformis* (Galloway and Wissler, 1927)	250	3.3	9.5	2.3	4.1	4	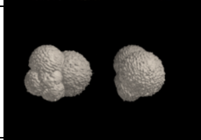	*Globigerinella obesa* (Bolli, 1957)	539	2.8	9.4	3.2	4.1	4
	*Neogloboquadrina humerosa* (Takayanagi & Saito, 1962)	360	5.0	22.7	2.0	2.4	4		*Globorotalia praemenardii (*Cushman & Stainforth, 1945)	569	3.9	14.0	2.0	3.2	4
	*Globoconella inflata* (d'Orbigny, 1839)	422	3.9	21.4	2.5	2.5	4	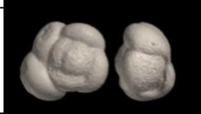	*Globoconella puncticulata* (d'Orbigny in Deshayes, 1832)	269	4.0	14.5	2.8	3.1	3
	*Fohsella lobata* (Bermúdez, 1949)	312	4.2	13.1	1.5	3.3	3		*Fohsella robusta* (Bolli, 1950)	312	3.5	11.2	2.3	3.7	4
	*Globorotalia margaritae (*Bolli & Bermúdez, 1965)	258	2.9	8.1	2.8	4.6	3	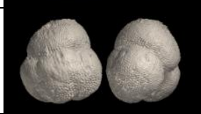	*Dentoglobigerina tripartita* (Koch, 1926)	303	5.7	33.6	2.0	1.9	3
	*Paragloborotalia mayeri* (Cushman & Ellisor, 1939)	298	3.1	8.1	3.2	4.5	4		*Paragloborotalia siakensis* (LeRoy, 1939)	366	3.4	10.4	2.6	3.9	4
	*Globoturborotalita nepenthes* (Todd, 1957)	353	4.2	16.4	2.4	2.9	3	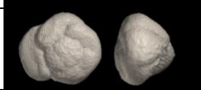	*Globoconella sphericomiozea* (Walters, 1965)	627	4.3	18.8	2.3	2.7	4
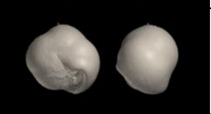	*Pulleniatina obliquiloculata* (Parker & Jones, 1865)	350	4.1	24.6	2.1	2.3	3	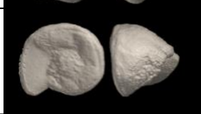	*Globorotalia (Truncorotalia) truncatulinoides* (d'Orbigny, 1839)	325	6.3	42.4	1.5	1.6	6
	*Fohsella peripheroronda* (Blow & Banner, 1966)	422	3.6	10.1	2.4	4.0	3	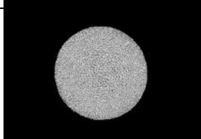	*Orbulina universa*[1] (d'Orbigny, 1839)	567	1.0	3.3	10.7	8.7	6
	*Praeorbulina curva* (Blow, 1956)	433	4.8	17.8	2.2	2.8	3								

468

Our predicted sinking speeds of foraminifera fall within aggregated existing data for 14 species (**Error! Reference source not found.**, Fok-Pun & Komar, 1983; Takahashi & Be, 1984; Caromel et al., 2014) and compare well with known speeds for other particles of comparable size and density (e.g. faecal pellets, (Table 3, Iversen & Ploug, 2010), phytoplankton (Fig. 1 in Smayda, 1971)). However, it should be noted that our predicted speeds are higher than published values for five out of the seven foraminifera species for which direct comparisons are possible (**Error! Reference source not found.**). This could be due to our ability to observe enlarged models of sinking foraminifera more accurately compared to actual specimens, and the lack of control for wall effects in previous work, which would tend to underestimate sinking speeds. There could also be considerable natural variation, which our single specimen per species (excluding *S. dehiscens*) does not capture.

Sedimentation of microscale plankton has been measured both *in situ* (e.g. Waniek, Koeve and Prien, 2000) and in the laboratory (e.g. Smayda, 1971; Miklasz and Denny, 2010). By settling dense suspensions of microorganisms, these studies provided a population sinking rate (Bienfang, 1981) which could be two to three times lower than the settling velocity of an isolated particle in the typically dilute ocean (Miklasz & Denny 2010). Other studies have, like us, used enlarged models of microscale plankton to facilitate observations. Padisak et al. (2003) used handmade models of plankton to examine drag, but there was no attempt at accurately matching Re. Holland (2010) used mechanical pencil leads as models of sinking diatom chains, keeping Re < 1 in an improvement over Padisak et al. (2003). However, neither authors calculated sinking velocities for real organisms. Our dynamic scaling approach ensures that we accurately recreate the fluid flows around settling organisms – a requirement for the correct prediction of sinking speeds. We also improve on previous methodologies by effectively eliminating wall effects, basing our models on µCT scans, and using inexpensive cameras to observe natural sinking orientation.

By design, our dynamic scaling approach yields an interpolated $C_D(Re)$ curve that describes the flow dynamics (and thus sinking speeds) that would occur if various fluid and/or particle parameters were varied, offering a degree of flexibility not seen in other studies. For example, phytoplankton blooms can increase both the density and viscosity of water due to exudates (Jenkinson et al., 2015), while increasing global temperatures have the opposite effect. The density and viscosity of seawater also naturally vary with latitude. Understanding how these variations affect sinking rates can offer insights into the evolutionary pressures on plankton. Our approach also allows us to isolate the effects of shape on sinking, even across species of widely varying size, density, etc, by comparing C_D of different species all hypothetically sinking at the same Re; a manuscript focused on such biological questions relating to foraminifera is currently in preparation. Differential settling speeds of foraminfera also have implications for nutrient cycling, paleoclimate reconstruction (Kucera, 2007), and the marine calcite budget (Schiebel, 2002).

Our method can easily be modified to study sedimenting particles operating at any Re, providing the system's Re range can be experimentally replicated. Other sinking marine particles include diatoms ($Re \approx 10^{-2}$ - 1,Botte, Ribera D'Alcalà and Montresor, 2013) and radiolaria ($Re \approx 10$ - 200,Takahashi and Honjo, 1983), for which one could use digital models as we have in conjunction with a suitably viscous fluid (high viscosity silicone oil, see SI Further Applications) to enable sufficiently large models to be produced (25 cm, see SI: Further Applications). The method can also be applied to terrestrial systems such as settling spores ($Re \approx 50$ e.g. Noblin, Yang and Dumais, 2009) and dispersing seeds ($Re \approx 10^3$ Azuma and Yasuda, 1989), again by using 3D printed models based on (often existing) µCT data.

Whilst our method pertains to settling in a quiescent fluid, one could conduct similar experiments using a flume to calculate threshold resuspension velocities (i.e. the horizontal flow speed required to lift a particle off the substrate), important in the study of wind erosion and particle transport and deposition (Bloesch, 1995; Bagnold, 1971). Similarly, studying particles suspended in shear flow could be achieved using a treadmill-like device (e.g. Durham et al (2009)) or a Taylor-Couette apparatus (e.g. Karp-Boss & Jumars (1998)). While additional dimensionless groups beyond Re and C_D would need to be matched to achieve similitude in these systems, we hope that our study provides a starting point for the experimental study of these and other more complex problems.

Acknowledgements

Our thanks go to Michael Kucera for supplying samples of planktonic foraminifera. For scanning three foraminifera at high resolution, this was supported by a grant from the Deutsches Elektronen-Synchrotron (DESY: I-20140099-EC) to Michael Fagan and Alexander Blanke. We thank Alex Blanke for preparing the samples and taking them to Hamburg. We also thank the rest of the Physical Ecology Lab (School of Life Sciences, University of Lincoln) members (Òscar Guadayol i Roig, Fouad El Baidouri, Mariona Segura, Jackson Sage and Sei Suzuki-Teller) for their support and help during the project. Our thanks go to Gregory Sutton and David Smith for their comments on a draft of this manuscript and we also thank Mark Denny and two other anonymous reviewers for their comments.

Competing interests

The authors have no competing interests to declare.

Author contributions

SH & MW were responsible for conceptualisation of the project, MW, SH and RS contributed to developing the methodology, MW collected data and JUH & FW scanned the three foraminifera at high resolution (See Table 1). RS & MW were responsible for MATLAB code, data curation and visualisation, formal validation of the method and the initial draft of the manuscript. TH segmented the high resolution scans, generated models used for 3D printing, and assisted with 3D printing of all models. MW, SH & RS contributed to editing and reviewing the manuscript, FW & JUH provided detials on methodology of high resoltuion scanning. SH & RS supervised MW for the duration of the project, and SH provided funding, resources and administration for the project.

Funding

All research was funded by Leverhulme Trust, Grant/Award Number: RL-2012- 022 awarded to SH.
High resolution scanning funded under Proposal I-20140099 EC awarded to Prof Michael Fagan and Dr Alex Blanke.

References

Ali, A., Thiem, Ø. & Berntsen, J. (2011). Numerical modelling of organic waste dispersion from fjord located fish farms. Ocean Dynamics. [Online]. 61 (7). p.pp. 977–989. Available from: http://link.springer.com/10.1007/s10236-011-0393-8.

Azuma, A. & Yasuda, K. (1989). Flight performance of rotary seeds. Journal of Theoretical Biology. [Online]. 138 (1). p.pp. 23–53. Available from: https://linkinghub.elsevier.com/retrieve/pii/S0022519389801766.

Bagnold, R.A. (1971). The Physics of Blown Sand and Desert Dunes. Dover Earth Science. [Online]. Dordrecht: Springer Netherlands. Available from: http://link.springer.com/10.1007/978-94-009-5682-7.

Batchelor, G.K. (2000). An Introduction to Fluid Dynamics. [Online]. Cambridge University Press. Available from: https://www.cambridge.org/core/product/identifier/9780511800955/type/book.

Berger, W.H., & Piper, D.J.W.W., (1972). Planktonic Foraminifera: Differential Settling, Dissolution, and Redeposition. Limnology and Oceanography. [Online]. 17 (2). p.pp. 275–287. Available from: http://doi.wiley.com/10.4319/lo.1972.17.2.0275.

Bienfang, P.K. (1981). SETCOL — A Technologically Simple and Reliable Method for Measuring Phytoplankton Sinking Rates. Canadian Journal of Fisheries and Aquatic Sciences. [Online]. 38 (10). p.pp. 1289–1294. Available from: http://www.nrcresearchpress.com/doi/10.1139/f81-173.

Bloesch, J. (1995). Mechanisms, measurement and importance of sediment resuspension in lakes. Marine and Freshwater Research. [Online]. 46 (1). p.p. 295. Available from: http://www.publish.csiro.au/?paper=MF9950295.

Booth, J.D. (1983). Studies on twelve common bivalve larvae, with notes on bivalve spawning seasons in New Zealand. New Zealand Journal of Marine and Freshwater Research. [Online]. 17 (3). p.pp. 231–265. Available from: http://www.tandfonline.com/doi/abs/10.1080/00288330.1983.9516001.

Botte, V., Ribera D'Alcalà, M. & Montresor, M. (2013). Hydrodynamic interactions at low Reynolds number: An overlooked mechanism favouring diatom encounters. Journal of Plankton Research. [Online]. 35 (4). p.pp. 914–918. Available from: http://academic.oup.com/plankt/article/35/4/914/1529648/Hydrodynamic-interactions-at-low-Reynolds-number.

Callieri, M., Ranzuglia, G., Dellepiane, M., Cignoni, P. & Scopigno, R. (2012). Meshlab as a Complete Open Tool for the Integration of Photos and Colour with High- Resolution 3D Geometry Data. Computer Applications and Quantitative Methods in Archaeology. p.pp. 406–416.

Caromel, A.G.M., Schmidt, D.N., Phillips, J.C. & Rayfield, E.J. (2014). Hydrodynamic constraints on the evolution and ecology of planktic foraminifera. Marine Micropaleontology. [Online]. 106. p.pp. 69–78. Available from: http://linkinghub.elsevier.com/retrieve/pii/S037783981400005X. [Accessed: 28 September 2014].

Clift, R., Grace, J.R. & Weber, M.E. (1978). Bubbles, Drops and Particles. New York: Academic Press.

D'Errico, J. (2009). SLM - Shape Language Modeling. [Online]. 2009. MATLAB Central File Exchange. Available from: http://www.mathworks.co.uk/matlabcentral/fileexchange/24443-slm-shape-language-modeling.

Durham, W.M., Kessler, J.O. & Stocker, R. (2009). Disruption of Vertical Motility by Shear Triggers Formation of Thin Phytoplankton Layers. Science. [Online]. 323 (5917). p.pp. 1067–1070. Available from: https://www.sciencemag.org/lookup/doi/10.1126/science.1167334.

Fayon, A.M. & Happel, J. (1960). Effect of a cylindrical boundary on a fixed rigid sphere in a moving viscous fluid. AIChE Journal. [Online]. 6 (1). p.pp. 55–58. Available from: http://doi.wiley.com/10.1002/aic.690060111.

Fok-Pun, L. & Komar, P.D. (1983). Settling velocities of planktonic foraminifera; density variations and shape effects. The Journal of Foraminiferal Research. [Online]. 13 (1). p.pp. 60–68. Available from: https://pubs.geoscienceworld.org/jfr/article/13/1/60-68/76175.

Gómez-Noguez, F., Pérez-García, B., Mehltreter, K., Orozco-Segovia, A. & Rosas-Pérez, I. (2016). Spore mass and morphometry of some fern species. Flora: Morphology, Distribution, Functional Ecology of Plants. [Online]. 223. p.pp. 99–105. Available from: http://dx.doi.org/10.1016/j.flora.2016.05.003.

Greving, I., Wilde, F., Ogurreck, M., Herzen, J., Hammel, J.U., Hipp, A., Friedrich, F., Lottermoser, L., Dose, T., Burmester, H., Müller, M. & Beckmann, F. (2014). P05 imaging beamline at PETRA III: first results. In: S. R. Stock (ed.). Developments in X-Ray Tomography IX. [Online]. 12 September 2014, San Diego, CA: SPIE, p. 92120O. Available from: https://doi.org/10.1117/12.2061768.

Guadayol, Ò. (2016). Trackbac. [Online]. Available from: https://zenodo.org/record/45559#.W6z6c2j0nIU.

Guadayol, Ò., Thornton, K.L. & Humphries, S. (2017). Cell morphology governs directional control in swimming bacteria. Scientific Reports. [Online]. 7 (1). p.p. 2061. Available from: http://www.nature.com/articles/s41598-017-01565-y.

B. K. Sen Gupta (ed.) (2002). Modern Foraminifera. Kluwer Academic Publishers.

Haibel, A., Ogurreck, M., Beckmann, F., Dose, T., Wilde, F., Herzen, J., Müller, M., Schreyer, A., Nazmov, V., Simon, M., Last, A. & Mohr, J. (2010). Micro- and nano-tomography at the GKSS Imaging Beamline at PETRA III. In: S. R. Stock (ed.). [Online]. 19 August 2010, p. 78040B. Available from: http://proceedings.spiedigitallibrary.org/proceeding.aspx?doi=10.1117/12.860852.

Happel, J. & Brenner, H. (1983). Low Reynolds number hydrodynamics with special applications to particulate media. Third. The Hague: Martin Nijhoff Publishers a member of Kluwer Academic Publishers Group.

Hayward, B.W., Le Coze, F. & Gross, O. (2018). World Foraminifera Database. [Online]. 2018. Available from: http://www.marinespecies.org/foraminifera/. [Accessed: 23 September 2020].

Holland, D.P. (2010). Sinking rates of phytoplankton filaments orientated at different angles: theory and physical model. Journal of Plankton Research. [Online]. 32 (9). p.pp. 1327–1336. Available from: https://academic.oup.com/plankt/article-lookup/doi/10.1093/plankt/fbq044.

Huesman, R.H., Gullberg, W.L., Greenberg, W.L. & Budinger, T.F. (1977). RECLBL Users Manual: Donner Algorithms for Reconstruction Tomography. [Online]. Available from: https://escholarship.org/uc/item/1mz679x3#main.

Iversen, M.H. & Ploug, H. (2010). Ballast minerals and the sinking carbon flux in the ocean: Carbon-specific respiration rates and sinking velocity of marine snow aggregates. Biogeosciences. 7 (9). p.pp. 2613–2624.

Jenkinson, I.R., Sun, X. & Seuront, L. (2015). Horizons: Thalassorheology, organic matter and plankton: Towards a more viscous approach in plankton ecology. Journal of Plankton Research. 37 (6). p.pp. 1100–1109.

Jones, R., Ricardo, G.F. & Negri, A.P. (2015). Effects of sediments on the reproductive cycle of corals. Marine Pollution Bulletin. [Online]. 100 (1). p.pp. 13–33. Available from: http://dx.doi.org/10.1016/j.marpolbul.2015.08.021.

Jonkers, L. & Kučera, M. (2015). Global analysis of seasonality in the shell flux of extant planktonic Foraminifera. Biogeosciences. [Online]. 12 (7). p.pp. 2207–2226. Available from: http://www.biogeosciences.net/12/2207/2015/.

Karamanev, D.G. (1996). Equations for calculation of the terminal velocity and drag coefficient of solid spheres and gas bubbles. Chemical Engineering Communications. 147. p.pp. 75–84.

Karp-Boss, L. & Jumars, P.A. (1998). Motion of diatom chains in steady shear flow. Limnology and Oceanography. [Online]. 43 (8). p.pp. 1767–1773. Available from: http://doi.wiley.com/10.4319/lo.1998.43.8.1767.

Kim, M.J., Bird, J.C., Van Parys, A.J., Breuer, K.S. & Powers, T.R. (2003). A macroscopic scale model of bacterial flagellar bundling. Proceedings of the National Academy of Sciences of the United States of America. 100 (26). p.pp. 15481–15485.

Koehl, M.A.R. (1995). Fluid flow through hair-bearing appendages: feeding, smelling, and swimming at low and intermediate Reynolds number. In: C. P. Ellington & T. J. Pedley (eds.). Biological Fluid Dynamics. Cambridge: The Company of Biologists Limited, pp. 157–182.

Koehl, M.A.R. (2003). Physical modelling in biomechanics J. van Leeuwen & P. Aerts (eds.). Philosophical Transactions of the Royal Society of London. Series B: Biological Sciences. [Online]. 358 (1437). p.pp. 1589–1596. Available from: http://www.pubmedcentral.nih.gov/articlerender.fcgi?artid=1693254&tool=pmcentrez&rendertype=abstract. [Accessed: 27 October 2014].

Kucera, M. (2007). Chapter Six Planktonic Foraminifera as Tracers of Past Oceanic Environments. In: Developments in Marine Geology. [Online]. London: Elsevier, pp. 213–262. Available from: http://linkinghub.elsevier.com/retrieve/pii/S1572548007010111.

De La Rocha, C.L. & Passow, U. (2007). Factors influencing the sinking of POC and the efficiency of the biological carbon pump. Deep Sea Research Part II: Topical Studies in Oceanography. [Online]. 54 (5–7). p.pp. 639–658. Available from: https://linkinghub.elsevier.com/retrieve/pii/S0967064507000392.

Lohmann, G.P. (1983). Eigenshape analysis of microfossils: A general morphometric procedure for describing changes in shape. Journal of the International Association for Mathematical Geology. 15 (6). p.pp. 659–672.

Mcandrew, A. (2004). An Introduction to Digital Image Processing with Matlab Notes for SCM2511 Image Processing 1 Semester 1 , 2004.

Miklasz, K.A. & Denny, M.W. (2010). Diatom sinkings speeds: Improved predictions and insight from a modified Stokes' law. Limnology and Oceanography. [Online]. 55 (6). p.pp. 2513–2525. Available from: http://doi.wiley.com/10.4319/lo.2010.55.6.2513.

Morard, R., Quillévéré, F., Escarguel, G., de Garidel-Thoron, T., de Vargas, C. & Kucera, M. (2013). Ecological modeling of the temperature dependence of cryptic species of planktonic Foraminifera in the Southern Hemisphere. Palaeogeography, Palaeoclimatology, Palaeoecology. [Online]. 391. p.pp. 13–33. Available from: http://dx.doi.org/10.1016/j.palaeo.2013.05.011.

Morrison, F.A. (2013). An Introduction to Fluid Mechanics. Cambridge: Cambridge University Press.

Morrison, F.A. (2010). Data correlation for drag coefficient for sphere. Michigan Technology University, Houghton, MI. [Online]. 6 (April). p.pp. 1–2. Available from: http://www.chem.mtu.edu/~fmorriso/DataCorrelationForSphereDrag2013.pdf.

Munson, B.R., Young, D.F. & Okiishi, T.H. (1994). Fundamentals of Fluid Mechanics. Second. New York: John Wiley and Sons, Inc.

Noblin, X., Yang, S. & Dumais, J. (2009). Surface tension propulsion of fungal spores. Journal of Experimental Biology. 212 (17). p.pp. 2835–2843.

Oskui, S.M., Bhakta, H.C., Diamante, G., Liu, H., Schlenk, D. & Grover, W.H. (2017). Measuring the mass, volume, and density of microgram-sized objects in fluid. PLoS ONE. 12 (4). p.pp. 1–17.

Padisák, J., Soróczki-Pintér, É. & Rezner, Z. (2003). Sinking properties of some phytoplankton shapes and the relation of form resistance to morphological diversity of plankton – an experimental study. Hydrobiologia. [Online]. 500 (1–3). p.pp. 243–257. Available from: http://link.springer.com/10.1023/A:1024613001147.

Passow, U. & Carlson, C. a. (2012). The biological pump in a high CO2 world. Marine Ecology Progress Series. 470 (2). p.pp. 249–271.

Purcell, E.M. (1977). Life at low Reynolds number. American Journal of Physics. 45 (1). p.pp. 3–11.

Reidenbach, M.A., George, N. & Koehl, M.A.R. (2008). Antennule morphology and flicking kinematics facilitate odor sampling by the spiny lobster, Panulirus argus. Journal of Experimental Biology. [Online]. 211 (17). p.pp. 2849–2858. Available from: http://jeb.biologists.org/cgi/doi/10.1242/jeb.016394.

Schiebel, R. (2002). Planktic foraminiferal sedimentation and the marine calcite budget. Global Biogeochemical Cycles. [Online]. 16 (4). p.pp. 3-1-3–21. Available from: http://doi.wiley.com/10.1029/2001GB001459.

Schiebel, R. & Hemleben, C. (2005). Modern planktic foraminifera. Paläontologische Zeitschrift. [Online]. 79 (1). p.pp. 135–148. Available from: http://link.springer.com/10.1007/BF03021758.

Van Sebille, E., Scussolini, P., Durgadoo, J. V., Peeters, F.J.C.C., Biastoch, A., Weijer, W., Turney, C., Paris, C.B. & Zahn, R. (2015). Ocean currents generate large footprints in marine palaeoclimate proxies. Nature Communications. [Online]. 6 (Ivm). p.p. 6521. Available from: http://dx.doi.org/10.1038/ncomms7521.

Smayda, T.J. (1971). Normal and accelerated sinking of phytoplankton in the sea. Marine Geology. 11 (2). p.pp. 105–122.

Sowa, Y. & Berry, R.M. (2008). Bacterial flagellar motor. Quarterly Reviews of Biophysics. [Online]. 41 (2). p.pp. 103–132. Available from: https://www.cambridge.org/core/product/identifier/S0033583508004691/type/journal_article.

Stacey, M.T., Mead, K.S. & Koehl, M.A.R. (2002). Molecule capture by olfactory antennules: Mantis shrimp. Journal of Mathematical Biology. [Online]. 44 (1). p.pp. 1–30. Available from: http://link.springer.com/10.1007/s002850100111.

Stadler, A.T., Vihar, B., Günther, M., Huemer, M., Riedl, M., Shamiyeh, S., Mayrhofer, B., Böhme, W. & Baumgartner, W. (2016). Adaptation to life in aeolian sand: how the sandfish lizard, Scincus scincus , prevents sand particles from entering its lungs. The Journal of Experimental Biology. [Online]. 219 (22). p.pp. 3597–3604. Available from: http://jeb.biologists.org/lookup/doi/10.1242/jeb.138107.

Sutton, M.D., Garwood, R.J., Siveter, D.J. & Siveter, D.J. (2012). SPIERS and VAXML; A software toolkit for tomographic visualisation and a format for virtual specimen interchange. Paleontologica electronica. 15 (2). p.pp. 1–15.

Takahashi, K. & Be, A.W.H. (1984). Planktonic foraminifera: factors controlling sinking speeds. Deep Sea Research Part A. Oceanographic Research Papers. [Online]. 31 (12). p.pp. 1477–1500. Available from: https://linkinghub.elsevier.com/retrieve/pii/0198014984900839.

Takahashi, K. & Honjo, S. (1983). Radiolarian skeletons: size, weight, sinking speed, and residence time in tropical pelagic oceans. Deep Sea Research Part A. Oceanographic Research Papers. [Online]. 30 (5). p.pp. 543–568. Available from: https://linkinghub.elsevier.com/retrieve/pii/0198014983900882.

Vogel, S. (1987). Flow-Assisted Mantle Cavity Refilling in Jetting Squid. The Biological Bulletin. [Online]. 172 (1). p.pp. 61–68. Available from: https://www.journals.uchicago.edu/doi/10.2307/1541606.

Vogel, S. (1994). Life in Moving Fluids. Second. Princeton, N.J., N.J.: Princeton University Press.

Vogel, S., Ellington, C.P. & Kilgore, D.L. (1973). Wind-induced ventilation of the burrow of the prairie-dog,Cynomys ludovicianus. Journal of comparative physiology. [Online]. 85 (1). p.pp. 1–14. Available from: http://link.springer.com/10.1007/BF00694136.

Vogel, S. & LaBarbera, M. (1978). Simple Flow Tanks for Research and Teaching. BioScience. [Online]. 28 (10). p.pp. 638–643. Available from: https://academic.oup.com/bioscience/article-lookup/doi/10.2307/1307394.

Waldrop, L.D., Reidenbach, M.A. & Koehl, M.A.R. (2015). Flexibility of crab chemosensory sensilla enables flicking antennules to sniff. Biological Bulletin. 229 (2). p.pp. 185–198.

Walsby, A.E. & Holland, D.P. (2006). Sinking velocities of phytoplankton measured on a stable density gradient by laser scanning. Journal of The Royal Society Interface. [Online]. 3 (8). p.pp. 429–439. Available from: https://royalsocietypublishing.org/doi/10.1098/rsif.2005.0106.

Waniek, J., Koeve, W. & Prien, R.D. (2000). Trajectories of sinking particles and the catchment areas above sediment traps in the northeast Atlantic. Journal of Marine Research. [Online]. 58 (6). p.pp. 983–1006. Available from: http://hermia.ingentaselect.com/vl=6505216/cl=63/nw=1/rpsv/cw/jmr/00222402/v58n6/s6/p983.

Wilde, F., Ogurreck, M., Greving, I., Hammel, J.U., Beckmann, F., Hipp, A., Lottermoser, L., Khokhriakov, I., Lytaev, P., Dose, T., Burmester, H., Müller, M. & Schreyer, A. (2016). Micro-CT at the imaging beamline P05 at PETRA III. AIP Conference Proceedings. 1741 (July).

Willson, M.F., Rice, B.L. & Westoby, M. (1990). Seed dispersal spectra: a comparison of temperate plant communities. Journal of Vegetation Science. [Online]. 1 (4). p.pp. 547–562. Available from: http://doi.wiley.com/10.2307/3235789.

Zohuri, B. (2015). Dimensional Analysis and Self-Similarity Methods for Engineers and Scientists. [Online]. Cham: Springer International Publishing. Available from: http://link.springer.com/10.1007/978-3-319-13476-5

Figure & Table Legends

Figure 1

Fig. 1.A) Diagram of relevant forces and parameters between the model (left) and real life (right). B) Summary of the full method; details are discussed in main text. Boxes with thicker lines represent a decision, square boxes are data inputs, rounded square boxes are manual processes, and circles are computational steps.

Figure 2

Fig. 2 A) Comparison of our empirically generated $C_D^E(Re)$ curve for 3D printed spheres versus the theoretical $C_D^M(Re)$ curve (Morrison, 2010) . Goodness of fit of $C_D^E(Re)$ to $C_D^M(Re)$ is $R^2 = 0.857$. Sphere diameter is indicated for each model. C & D) An example of our iterative solution process for C. dissimilis showing best estimates of operating values (including the required model scale S to achieve similitude) based on experimental data from 3 (C), vs 4 (D) models. For reference, the theoretical $C_D^M(Re)$ curve (Morrison, 2010) for a sphere is also shown. In C, S corresponding to the operating point is estimated as 13.84. After an additional model was sunk at S = 13 (D), slightly more accurate estimates of the operating S, Re^O, and C_D^O were obtained. When scaling the model for 3D printing only 1 decimal place was used rather than the 2 shown. D-I) Models of foraminifera 3D printed in clear and black resin. Models were used for public engagement but demonstrate the fidelity of the printer compared to the scan data shown Table 1.

Table 1

Table 1.Predicted sinking speeds U^O for the 30 species of planktonic foraminifera included in this study, with each species shown in both spiral view and 90˚ rotation (so that the spiral view is facing to the left). [1] indicates species scanned high resolution. Scans of the remaining 27 species were obtained from The University of Tohoku museum's database. Operating Re^O and C_D^O predicted for each species are also presented, and for comparison, the theoretical C_D^M of a sphere at the same Re^O. The number of model iterations required to achieve convergence of U^O is listed (iter). Species synonyms checked at World Foramaninifera Database (Hayward et al., 2018).